Measurement of the fluorescence decay rate of $2\,^3P_J$ positronium

R. J. Daly, R. E. Sheldon, and D. B. Cassidy
Department of Physics and Astronomy, University College London, Gower Street, London WC1E 6BT, United Kingdom

(Received 4 June 2024; accepted 15 July 2024; published 12 August 2024)

The fluorescence decay rate of $2\,^3P_J$ positronium (Ps) atoms [$\Gamma_{\rm fl}$] has been experimentally determined using a Stark-mixing technique. Ground-state Ps atoms were optically excited in an electric field to states containing both $2\,^3P_J$ and $2\,^3S_1$ components. The relative state populations were controlled via an applied mixing electric field, and a larger, pulsed, electric field was used to induce rapid quenching of the system after a fixed time delay. The dependence of the quenching signal on the mixing field strength was used to determine the relative S and P populations of the mixed states, whose decay rates are determined by the intrinsic self-annihilation and fluorescence decay rates. The measurements were compared to a trajectory simulation and Stark-mixing model, using the fluorescence decay rate as a free parameter. By finding the best agreement between the data and simulations we obtain $\Gamma_{\rm fl} = 299 \pm 25\ \mu{\rm s}^{-1}$, which is consistent with the mean theoretical value of $313.343 \pm 0.003\ \mu{\rm s}^{-1}$.

DOI: 10.1103/PhysRevA.110.022807

I. INTRODUCTION

Positronium (Ps), the bound state of an electron and a positron [1], is a hydrogenic atomic system composed only of leptons, and as such is well suited for testing bound-state QED theory [2]. Such tests are performed by comparing measured properties of Ps with quantities that can be calculated with high precision, such as intervals between atomic energy levels or self-annihilation decay rates [3]. Measurements of Ps energy intervals are performed via spectroscopic means, using microwave [4] or laser [5] radiation to drive transitions between levels. Decay rate measurements are generally performed by measuring stop and start times, corresponding to positron production and subsequent Ps annihilation [6].

Currently the most precise theory values for Ps decay rates are $\Gamma_{o\text{-Ps}} = 7.039979(19)\ \mu{\rm s}^{-1}$ for the triplet ground states ($1\,^3S_1$, o-Ps) and $\Gamma_{p\text{-Ps}} = 7.989618(18)\ {\rm ns}^{-1}$ for the singlet ground state ($1\,^1S_0$, p-Ps) [3]. This corresponds to mean lifetimes of ∼142 ns and 125 ps, respectively. The o-Ps decay rate has been measured many times and disagreement with theory was at one point the subject of some controversy, known as the positronium lifetime puzzle [7]. This has now been resolved [8,9], and measurements and theory are presently in good agreement; the average value of the new measurements is $\Gamma_{o\text{-Ps}} = 7.0401(11)\ \mu{\rm s}^{-1}$ [10]. Only the ground-state decay rates have been measured with high precision; the $n = 2$ triplet decay rate [11] and Rydberg Ps fluorescence decay rates [12] have been measured with a precision on the order of 10%.

The fast p-Ps decay rate $\Gamma_{p\text{-Ps}}$ is difficult to measure directly, and all experiments performed so far have relied upon a scheme in which singlet and triplet ground states are mixed in a magnetic field via the Zeeman effect. This produces a mixed state with a slower decay rate (longer lifetime) owing to the admixture of the o-Ps component, which means that the p-Ps decay rate can be obtained from measurements of the mixed-state decay rate if the triplet decay rate and the strength of the external mixing field are known [6]. Several measurements have been performed using this method [13–15]; the most precise value obtained is $\Gamma_{p\text{-Ps}} = 7.9909(1.7)\ {\rm ns}^{-1}$ [15], which is also in agreement with theory [3].

Self-annihilation is the only decay mode available for Ps atoms in the ground state, but excited-state atoms may also decay radiatively. The annihilation decay rate depends on the overlap of the electron-positron wave functions (i.e., $|\psi(0)|^2$) [16]. This means that, for all practical purposes, only S states decay via self-annihilation, and the decay rate scales with n^3. Thus, the corresponding $2\,^1S_0$ and $2\,^3S_1$ lifetimes are ∼1 ns and 1 μs, respectively. For $2P$ levels self-annihilation is highly suppressed because there is no wave-function overlap [17,18]. The situation is reversed for radiative decay, which is forbidden by electric dipole selection rules for the $2S$ levels, but not for $2P$ levels, which therefore decay exclusively via fluorescence. The corresponding radiative decay rate (averaged over all accessible $2\,^3P_J$ substates) is $313.343 \pm 0.003\ \mu{\rm s}^{-1}$ [16].

Since both S and P levels are present in the $n = 2$ manifold, electric fields can be used to mix them via the Stark effect, and thus produce states whose lifetimes depend on the applied electric field [19]. By performing measurements in different electric fields it is possible to determine the $2\,^3P_J$ radiative decay rate if the $2\,^3S_1$ annihilation decay rate is known; this method constitutes a Stark-mixing analog of the Zeeman-mixing method used to determine the p-Ps decay rate [15]. Here, we report the results of such a measurement. The basic methodology of the experiment is as follows: Ps

atoms, optically produced in the $2\,^3S_1$ level, enter a region in which an applied electric field mixes the $2\,^3S_1$ and $2\,^3P_J$ levels, producing a mixed state. A subsequent quenching pulse is then used to measure the remaining atom fraction after a fixed time delay. This is repeated for a range of mixing fields, and we then compare these measurements to simulations performed using a variable fluorescence decay rate $\Gamma_{\rm fl}$ to find the rate that gives the best agreement with the data. We obtain $\Gamma_{\rm fl} = 299 \pm 25\ \mu{\rm s}^{-1}$, which is consistent with the theoretical value.

II. EXPERIMENTAL METHODS

A. Positronium production and excitation

The experimental methods used to produce, excite, and detect Ps atoms in the present work are similar to those described elsewhere [20]. A dc positron beam formed from a ^{22}Na source and a neon moderator [21] was converted to a pulsed beam using a two-stage Surko-type buffer gas trap [22] and a harmonic buncher [23]. The apparatus produced positron pulses with spatial (temporal) widths of 3 mm (4 ns) (FWHM) containing $\sim 10^5$ positrons [20] at a repetition rate of 1 Hz. This beam was implanted into a mesoporous silica target [24], mounted on electrode T, with an implantation energy of $\sim$4 keV. The positron beam was magnetically guided by an axial field of strength 63 G. The time at which positrons were implanted into the target is defined as $t_0 = 0$, and other quoted times are in reference to this.

Ps atoms emitted into vacuum from the silica target were irradiated with pulsed laser light to excite either $2\,^3S_1$ [25] or Rydberg states [26], or to photoionize Ps atoms [20], as indicated in Fig. 1. Two dye lasers were used in the experiments [20]; a ultra violet (UV) laser propagating in the $+x$ direction ($\lambda = 243$ nm, $\Delta t = 4$ ns, $\Delta\nu \approx 100$ GHz, 0.5 mJ/pulse) and an infrared (IR) laser propagating in the $-x$ direction ($\lambda \approx 730$ nm, $\Delta t = 5$ ns, $\Delta\nu \approx 5$ GHz, 5 mJ/pulse). The IR and UV dye lasers were pumped by the second (532 nm) and third (355 nm) harmonics a single Nd:YAG (neodymium-doped yttrium aluminum garnet) laser, respectively. The pulsed lasers were fired at the optimal time for maximum Ps excitation, which was $t_l = 20$ ns.

As indicated in Fig. 1, Ps formation and laser excitation were conducted between electrodes T and E1, which were designed to control the local electric fields. This was designated the laser excitation region (LER), with an electrode separation of 7 mm. A third electrode (E2) was located 40 mm beyond E1. The space between E1 and E2 was designated the field mixing region (FMR). Both E1 and E2 contain high transmission (95%) tungsten meshes to allow positrons and Ps atoms to pass through.

For Ps production, the positron beam implantation energy was controlled by biasing T to $V_{\rm T} = -4.5$ kV, which resulted in an electric field in the LER of $F_{\rm ex} = 6.4$ kV/cm, with E1 held at ground potential. Some of the atoms produced in the LER were able to travel through E1 into the FMR, where a mixing electric field was applied by biasing E2. After a variable time delay t_Q, atoms in the FMR and LER were quenched by rapidly applying a large voltage pulse (+4 kV) to electrode E1 with a switch-on time (10%–90%) of 34 ns.

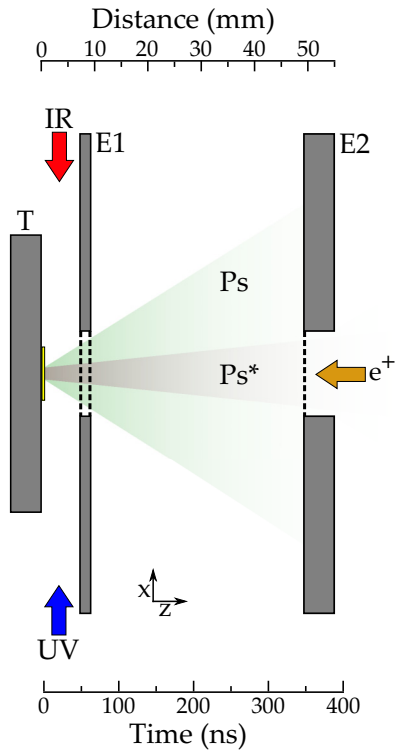

FIG. 1. A schematic representation of the electrode structure used in the experiment showing the target electrode (T) and the two electrodes used to define the field mixing region (E1 and E2). The upper scale indicates the electrode positions along the z axis. The corresponding travel time for Ps atoms moving in the z direction at the average velocity of 140 km/s is shown on the lower scale. The shaded cones indicate the trajectories of ground-state (Ps) and excited-state (Ps*) atoms. The blue (red) arrow indicates the direction of the UV (IR) laser.

A Stark-mixing production scheme (described in detail in Ref. [25]) was used to generate Ps atoms in the $2\,^3S_1$ level. The UV laser was used to drive $1\,^3S_1 \rightarrow 2\,S^*$ transitions in an electric field $F_{\rm ex}$, where $2\,S^*$ refers to a Stark mixed excited state [19]. Since $2\,S^*$ states contain both $2\,^3S_1$ and $2\,^3P_J$ components, rapidly switching off $V_{\rm T}$ (and hence $F_{\rm ex}$) allows the adiabatic evolution $2\,S^* \rightarrow 2\,^3S_1$ to occur. Using a fast high-voltage (HV) switch, $V_{\rm T}$ was switched to 0 V immediately after the excitation laser pulse. The voltage switch-off time $t_{\rm fall}$ (90%–10%) was 32 ns, which allowed approximately 5% of excited atoms to evolve to the pure $2\,^3S_1$ state [25]. We note that the presence of a magnetic field means that the states are not pure, and the $2\,^3S_1$ levels produced actually contain some singlet component. This lowers the lifetime slightly, but is negligible in the present work.

Positronium atoms in highly excited (Rydberg) states [27] were produced using two overlapping laser pulses (UV + IR). The UV laser was used to drive $1\,^3S_1 \rightarrow 2\,^3P_J$ transitions, as described above, and the IR laser was used to drive $2\,^3P_J \rightarrow n\,^3S/{\rm D}$ transitions [26]. Laser light with wavelength $\lambda = 734.6$ nm was used to generate Rydberg atoms with principal quantum number $n = 23$, which was verified by selective field ionization [28]. Measurements were also performed with the IR laser wavelength tuned to $\lambda = 728$ nm, which is above

the energy threshold for photoionization. This was used to measure the transverse Ps velocity distribution via Doppler spectroscopy [29].

Since it is easier to produce Rydberg atoms in a lower electric field to prevent field ionization or Stark broadening of the excitation line shape [30], the target bias for positron implantation was reduced to $V_T = -3.5$ kV for Rydberg excitation. This does not change the Ps emission energy [29], but can affect the mean Ps emission time from the silica target. Previous studies using a nominally identical silica film indicate that this difference is less than 3 ns [31] and can be safely neglected in the present work. The bias V_T, and hence the electric field in the LER, was switched off at time $t = 5$ ns, after the positron pulse was implanted, but before the UV and IR laser pulses were applied.

Measurements of Ps production, excitation, and decay processes were made via the time dependence of annihilation gamma radiation using a single-shot lifetime method [32]. Lifetime spectra $V(t)$ were recorded using four gamma ray detectors (D1–D4), each comprising a lutetium-yttrium oxyorthosilicate (LYSO) scintillator attached to a photomultiplier tube [33].

Background subtracted lifetime spectra were used to quantify the number of quenched $2S^*$ and field-ionized Rydberg atoms [11]. The $2S^*$ (Rydberg) spectra was subtracted from the quenched $2S^*$ (field-ionized Rydberg) spectra to produce an annihilation peak [e.g., Fig. 5(a)], the integrated area of which was proportional to the number of atoms present in the apparatus at the quenching time t_Q. An additional background subtraction was required to remove noise in the signal due to pick up in the detection system from the fast HV switch used to generate the quenching signals. Background subtracted lifetime spectra were normalized to the total integrated lifetime spectra area A_{AC} to compensate for variations in the positron beam intensity. The normalization integration was performed between the time windows $t_A = -30$ ns and $t_C = 1000$ ns to encompass all positron annihilation events resulting from positron implantation into the target.

By integrating the lifetime spectra we can obtain the parameter $f_d = \frac{A_{AC}-A_{AB}}{A_{AC}}$, where the time windows t_B and t_C are chosen according to the type of event being studied [20]. Photoionization and Rydberg production were characterized using the parameter S_γ, which is defined as $S_\gamma = \frac{f_{\rm off}-f_{\rm on}}{f_{\rm off}}$, where $f_{\rm on}$ ($f_{\rm off}$) refers to measurements made with the radiation source (i.e., laser) on (off).

B. Velocity distributions

The transverse Ps velocity distribution v_x was measured directly via Doppler spectroscopy [29]. An example of a Doppler profile measured via photoionization is shown in Fig. 2(a). The width of this line shape is dominated by Doppler broadening and is ∼835 GHz (FWHM), which is much larger than the 50 MHz (FWHM) natural width of the underlying $1\,^3S_1 \rightarrow 2\,^3P_J$ transition. This distribution represents the ground-state v_x distribution, which is the same as the v_y distribution, owing to the random pore structure of the silica target. The excited-state v_y^* distribution is the same as that of the ground state (i.e., $v_y^* = v_y$), but the excited-state v_x^* distribution is much narrower than the ground-state distribution v_x because it is limited by velocity selection from the ∼100 GHz bandwidth of the UV excitation laser. The corresponding v_y and v_x^* velocity distributions are shown in Fig. 2(b).

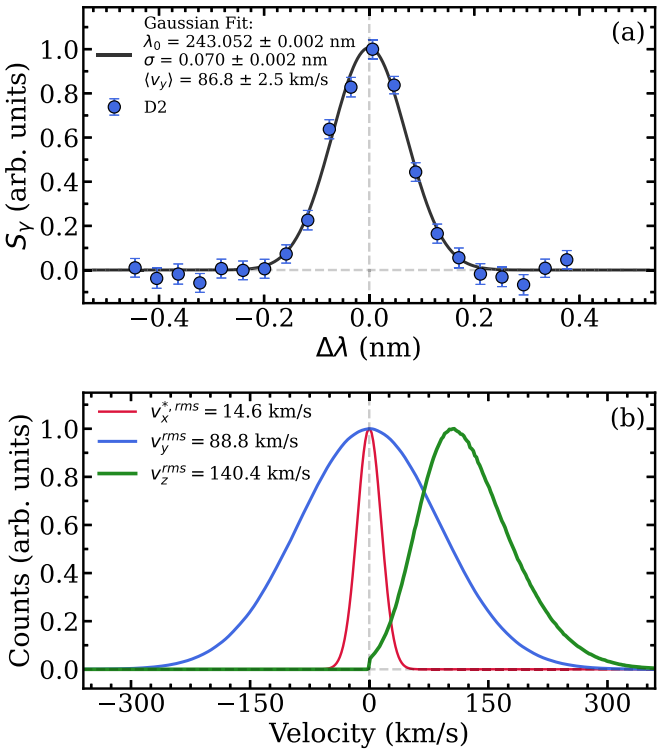

FIG. 2. (a) Measured spectral line shape of the $1\,^3S_1 \rightarrow 2\,^3P_J$ transition with integration bounds $t_B = 100$ ns and $t_C = 700$ ns. (b) The corresponding v_y velocity distribution. Also shown in (b) are the velocity-selected excited-state v_x^* distribution, as defined by the 100-GHz UV excitation laser bandwidth, and the excited-state v_z distribution obtained from time-delayed Rydberg ionization measurements (see Appendix). The legend shows the root-mean-square speeds for each indicated distribution.

The longitudinal Ps velocity distribution (v_z) was obtained using time-dependent Rydberg field ionization measurements. In these measurements Rydberg atoms excited to the $n = 23$ state were allowed to propagate for a variable time, after which they were ionized by the application of a large electric field [28]. The Rydberg atoms generated in this process have negligible annihilation decay rates, and their radiative lifetime is more than 40 μs [12], meaning that essentially no loss of Rydberg atoms will occur on the 1 μs timescale of the experiment. The velocity distributions of the excited-state atoms are largely determined by the ground-state distributions and the UV excitation laser properties [34]. Thus, the velocity distributions of the Rydberg Ps atoms are expected to be identical to those of the $2\,^3S_1$ atoms (excluding any changes in motion caused by external field gradients [35]).

The Ps time-dependent Rydberg field ionization measurements were compared to simulations including particle trajectories, local electric fields, and atom decay. These were run using a trial v_z distribution, obtained from time-of-flight measurements made using Rydberg atoms in a ring guide [36]. This distribution was then adjusted so as to minimize the difference between the simulations and the measured data

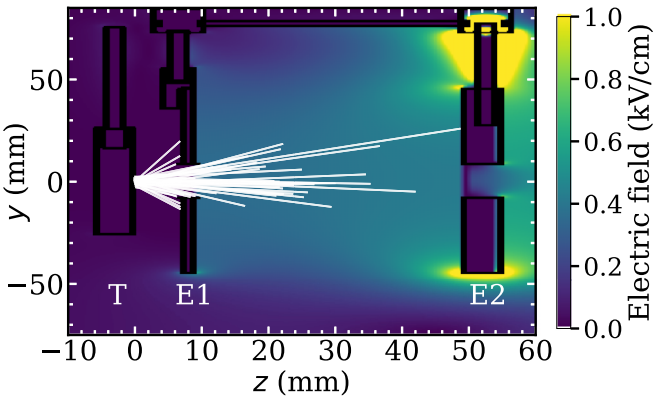

FIG. 3. Simulated trajectories of 100 $2S^*$ atoms traveling through the y-z plane ($x = 0$) of the electrode structure used in the experiments. The color map indicates the applied mixing electric field of ∼0.38 kV/cm, resulting from a bias of 1520 V applied to E2, with electrode E1 held at ground potential.

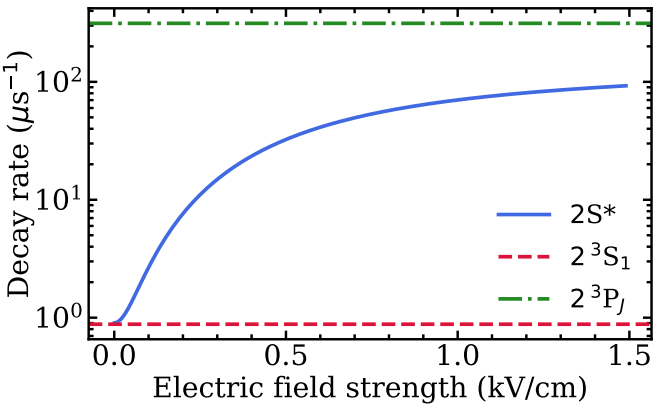

FIG. 4. Calculated decay rates of the $2S^*$ mixed state as function of applied electric field. The calculation also includes an axial magnetic field of strength 63 G to match the experimental conditions. The decay rate is almost exclusively determined by fluorescence decay to the ground state. The annihilation and fluorescence decay rates of the constituent $2\,^3S_1$ and $2\,^3P_J$ levels are also shown in the figure, indicated by the horizontal lines.

(see Appendix for details). The final v_z distribution obtained is shown in Fig. 2(b).

III. SIMULATIONS

Analysis of the experiment involved comparison of measured data with simulations. To generate the simulated data, Monte Carlo sampling methods were used to determine a set of Ps trajectories using the velocity distributions shown in Fig. 2(b). The starting coordinates and creation times of the Ps atoms were sampled from Gaussian distributions defined by the radial and temporal width of the incident positron beam. A total of 40 000 trajectories were generated per simulation to reduce the statistical error to negligible levels [37].

The stepwise trajectory for each atom was determined by a leapfrog algorithm, with a step interval of $dt = 2$ ns. The trajectories were terminated following annihilation events which occurred if Ps atoms (1) collided with objects in the vacuum system, (2) decayed by self-annihilation, or (3) encountered electric fields strong enough to cause ionization. The self-annihilation rates of atoms were determined by the atomic state and external electric fields, including fluorescence decay processes that transfer $2S^*$ atoms to the ground state [19]. Rydberg atoms were considered to be stable to self-annihilation, but could radiatively decay to the ground state.

Electric field distributions were calculated using the SIMION software package [38], which uses finite element methods (FEM) to evaluate the electric fields within a volume with user-specified electrode configurations. The simulated volume contained the three electrodes, their mounting mechanism, and the surrounding vacuum chamber, which were used as boundary conditions in the solver. Figure 3 shows typical particle trajectories in the electrode structure, as well as a two-dimensional (2D) color map representing the electric field configuration used for field mixing $2S^*$ atoms. In this example an electric field of ∼0.38 kV/cm is generated using applied voltages of $V_T = 0$ V, $V_{E1} = 0$ V, and $V_{E2} = 1520$ V.

Whether a quenching or ionization event occurred was determined in a Monte Carlo process by converting the appropriate field-dependent decay rate $\Gamma(F)$ to a probability $P = 1 - \exp[-\Gamma(F)dt]$, which was compared to a random number within each finite time step of the leapfrog propagation. The ionization rates for Rydberg atoms were determined by randomly selecting one of the k substates within the $n = 23$ manifold, assuming uniform distribution, for which the ionization rate can be calculated in any given electric field [27,28].

The decay rate for $n = 2$ Ps depends on external fields which mix S and P levels and opens the pathway for $2\,^3S_1$ to decay via fluorescence by adding some $2\,^3P_J$ character. Fluorescence and annihilation decay rates (Γ_{fl}, and Γ_{ann}, respectively) for Ps atoms in state i in external fields are given by

$$\Gamma_{fl,\,i} = \sum_j C_{i,j}^2\,\Gamma_{fl,\,j} \tag{1}$$

and

$$\Gamma_{ann,\,i} = \sum_j C_{i,j}^2\,\Gamma_{ann,\,j}, \tag{2}$$

where $C_{i,j}$ are the coefficients of the eigenvectors of the full Hamiltonian matrix (i.e., including the Zeeman and Stark components) and j is an index over all $n = 2$ basis states (see Ref. [19] for details). These coefficients depend on the applied fields, and the total decay rate for each eigenstate is given by

$$\Gamma_{tot,i} = \Gamma_{fl,i} + \Gamma_{ann,i}. \tag{3}$$

The present experiment was conducted in an axial magnetic field of strength $B_z = 63$ G. In this field, Zeeman mixing changes the $0.88\,\mu s^{-1}$ $2\,^3S_1$ lifetime to ∼0.90 μs^{-1} for the $2S^*$ mixed state. The calculated $2S^*$ decay rate due to various electric fields is shown in Fig. 4, including the Zeeman mixing for $B_z = 63$ G. We note that the large difference between the annihilation and fluorescence decay rates means that the measurement is very insensitive to the former, and that the magnetic field has a negligible impact on the final result.

As in the experiment, the V_{E1} quenching bias of 4 kV was applied at varying times, either to quench $2\,S^*$ atoms or field-ionize Rydberg atoms. The switching process of V_T was also included. These potentials, and the concomitant electric fields, did not appear instantaneously at the selected times, but instead were matched to the measured switch rise times of 32 ns and 34 ns (10%–90%) for V_T and V_{E1}, respectively. V_{E2} had no rise time as the mixing fields were not pulsed.

Lifetime spectra were generated by convolution of the simulated gamma flux with a detector response function that included the measured detector rise (5 ns) and decay (40 ns) times. These spectra were matched to data using arbitrary scaling factors, since the detector solid angles or other geometrical effects were not included in the simulations. Simulated lifetime spectra were generated for all experimental conditions, including a background simulation wherein the E1 pulse was not applied. By performing the same background subtraction on simulated spectra as were used with experimental data, an analog of the measured signals was generated that could be directly compared to data, as discussed in Sec. IV.

IV. RESULTS AND DISCUSSION

The main result of the experiments performed in this work are measurements of the number of $2\,S^*$ atoms surviving after experiencing mixing electric fields of varying strengths. These data were obtained by applying a quenching pulse at a fixed time ($t_Q = 190$ ns) relative to the production of excited-state Ps atoms. This quenching pulse resulted in rapid radiative decay to the ground state, and a subsequent increase in the gamma ray flux that is proportional to the number of remaining atoms. An example of such measurements (recorded using a single detector) is shown in Fig. 5(a). A simulation of this process was performed using the methods detailed in Sec. III, and the results are shown in Figs. 5(b) and 5(c). Both the measured and simulated data have been normalized to the maximum height of the quenching peaks. The curves show the signals for a range of mixing fields F_{mix}. It is evident that for larger fields, where more P character is present in the $2\,S^*$ state, fewer atoms remain at the quenching time, as one would expect.

The simulations shown in Figs. 5(b) and 5(c) include $2\,P$ fluorescence decay rates (Γ_{fl}) of 1000 and 200 μs^{-1}, respectively. Simulations of this type were performed for a wide range of Γ_{fl} values, with the goal of finding the Γ_{fl} that best matches the data. A direct comparison was made between the individual peak areas, which were determined by integrating the relevant background-subtracted spectra. The integration bounds were defined as the average time the rising and falling edge of the quenching peaks crossed $x = 0$ across all mixing fields. The bounds were uniquely determined for each detector and simulation to account for differences in detected events and Γ_{fl}, respectively.

The measured A_{exp} and simulated A_{sim} peak areas were then used to determine the reduced chi-square parameter between the model and the experimental data [39]:

$$\chi^2_{red} = \frac{1}{\nu}\sum\left(\frac{A_{exp} - A_{sim}}{\sigma_{exp}}\right)^2, \tag{4}$$

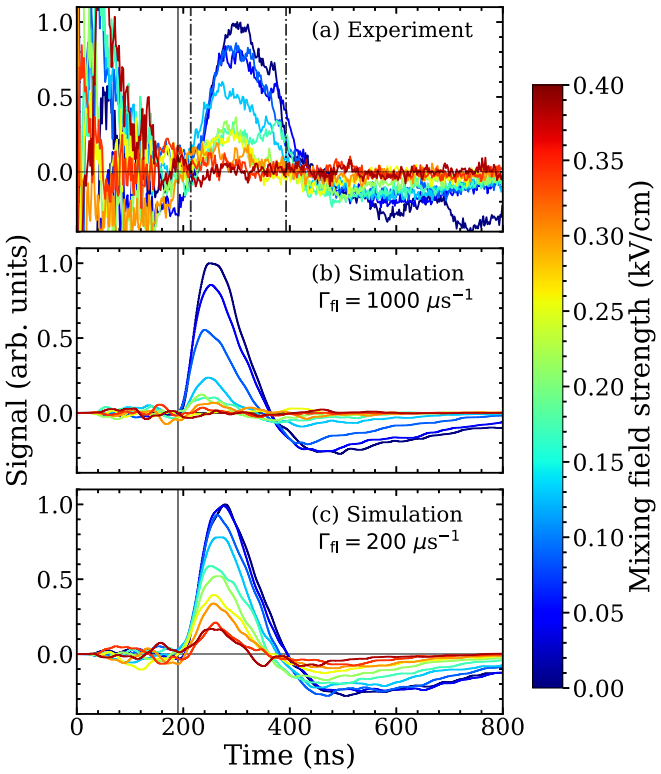

FIG. 5. Background subtracted $2\,S^*$ quenching data obtained using (a) detector D1, and simulations obtained using $2\,^3P_J$ decay rates of (b) 1000 μs^{-1} and (c) 200 μs^{-1}. Measurements were made using a range of electric potentials applied to E2, generating the electric field strengths indicated by the color map. The solid vertical line at 190 ns indicates the time at which the quenching pulses were applied. The dot-dashed lines in (a) indicate the integration bounds $t_1 = 214$ ns and $t_2 = 393$ ns used to calculate A_{exp} for D1.

where σ_{exp} is the error associated with A_{exp}, $\nu = N - F - 1$, N is the number of data points, and $F = 1$ is the number of degrees of freedom. χ^2_{red} was minimized for each recorded data set (i.e., data obtained from each detector).

The observed quenching peaks in Fig. 5(a) are slightly wider than the simulated peaks shown in Fig. 5(b). This may be caused by ringing in the HV switch; the maximum field applied is 1 kV/cm, which will increase the $2\,S^*$ decay rate to around 100 μs^{-1} (see Fig. 4), but field oscillations on this time scale could result in a partially delayed quenching signal. No such effect is observed, or would be expected, for the Rydberg ionization signal since the applied field is much larger than the ionization field. However, as even a delayed quenching peak area will be proportional to the number of surviving atoms, we expect the analysis described above to remain valid.

Figure 6 shows examples of χ^2_{red} as a function of Γ_{fl}, obtained for all four of the detectors used in the experiment. A polynomial function of the sixth order has been fitted to the data and used to define the minimum of the data sets. The sixth-order polynomial was the lowest-order fit function to be within 1% of the R^2 value of the preceding order polynomial, taken to be the point at which the fit to the data converges, where R^2 is the coefficient of determination [39]. The true value of Γ_{fl} is expected to correspond to the best match to

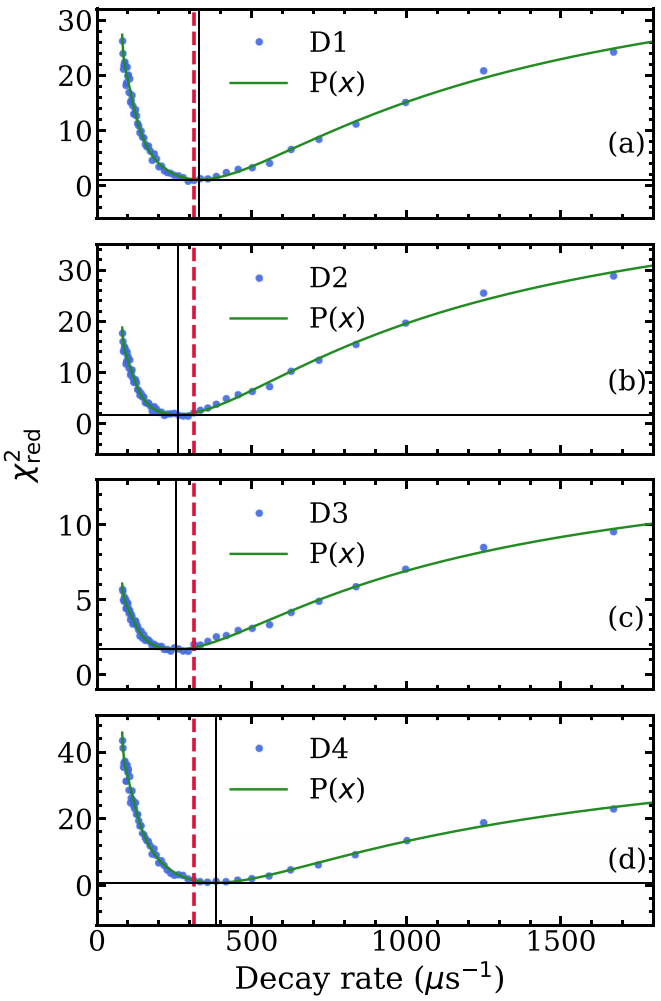

FIG. 6. $\chi^2_{\rm red}$ obtained for different $2\,^3P_J$ decay rates using the four LYSO detectors (D1–D4). A sixth-order polynomial function $P(x)$ was used to fit the data, from which the minima were determined. The dashed red vertical line indicates the theoretical decay rate value (313 μs^{-1}). The black vertical and horizontal lines correspond to the minima of the polynomial fits for each data set.

the data set, and hence to the minimum of $\chi^2_{\rm red}$. This minimization routine does not return a meaningful error bar on the obtained value of $\Gamma_{\rm fl}$; instead, we estimate the overall error using the standard error of the mean, obtained from averaging the results from the four detectors. We obtain a final result of $\Gamma_{\rm fl} = 299 \pm 25\ \mu$s^{-1}.

A measurement of the radiative decay rate of a particular Ps level constitutes an indirect measurement of the energy interval ν between the initial and final states involved in the decay process. Therefore, such measurements can, in principle, test QED theory. The fluorescence decay rate for transitions between levels with quantum numbers $n\ell$ and $n'\ell'$ is given by [16]

$$\Gamma_{n'\ell',n\ell} = \frac{2e^2\omega^3_{n'\ell',n\ell}}{3\epsilon_0 hc^3}\frac{\ell_{\rm max}}{2l+1}\langle n'\ell'|r|n\ell\rangle^2, \qquad (5)$$

where $\omega_{n'\ell',n\ell} = 2\pi\nu_{n'\ell',n\ell}$ is the angular frequency of the transition, $\ell_{\rm max} = \max(\ell, \ell')$ is the maximum angular quantum number of the two involved levels, and the other constants have the usual meanings. Using calculated Ps energy levels [3] and physical constants obtained from CODATA 2022 [40], the average decay rate of the $2\,^3P_J$ substates is 313.343 $\pm$ 0.003 μs^{-1}. This value comes from a weighted average over the energy differences between the $2\,^3P_J$ substates, which are not uniquely selected in this measurement. The weighting is 3:2:1 for the $J = 2$, $J = 1$, and $J = 0$ levels, respectively, based on the number of M_J sublevels [41]. The uncertainty in the calculated decay rates arising from QED corrections to the various $2\,^3S_1 \to 2P$ energy levels is extremely small (on the parts-per-billion scale) because it is dominated by the small uncertainty in the $1\,^3S_1 \to 2\,^3S_1$ interval.

The uncertainty arising from averaging over all $2\,^3P_J$ substates is much larger than that obtained from QED corrections or the errors in the CODATA constants, and a precision measurement would have to be conducted using only one $2\,^3P_J$ level. This could be achieved by using a high-power microwave pulse to depopulate specific M_J substates of the initial $2\,^3S_1$ ensemble [41] before atoms enter the mixing field, and then conducting measurements with various different Stark-mixed states. At the current level of precision our result is consistent with the theoretical value averaged over all states.

The precision of the experiment could be improved in several ways. The size of the FMR was chosen so that the detector solid angles would not be appreciably different for atoms quenched by the applied field. However, this also meant that not all Ps atoms were in the mixing region at the same time, and transport of atoms in and out of the FMR, as well as other effects, such as collisions, had to be taken into account via the simulations.

Using a slower, collimated Ps source and a large-area detector could remove or reduce these effects. This would allow for an analytical determination of the $2\,^3P_J$ decay rate, with no need to compare measured data to simulations. We could, in this way, directly measure the total mixed state decay rate [see Eq. (3)] as a function of the applied mixing field and also the time spent in these fields (by varying the pulse times). This would allow us to perform measurements with better control over systematics, and to obtain the concomitant error determination.

In the present work effects arising from the presence of a 63 G magnetic field were negligible, but could be fully eliminated by performing experiments in a field-free region [42]. The electronic noise associated with fast HV switching could be reduced with improved electronics and impedance matching with the electrode structures. Alternatively, the fraction of atoms surviving after traveling in the mixing field could instead be probed using a high-power microwave pulse to drive $2S^* \to 2\,^3P_2$ transitions in the FMR [43].

If all of these improvements were implemented we would expect substantial improvements to the achievable precision. However, it is difficult to predict exactly what degree of improvement could be achieved since it would depend on the (unknown) performance of the large area detector required to expand the mixing region. This would also allow direct lifetime measurements to be made in different electric fields. If a precision comparable to that obtained in the ground-state Ps decay rate measurements [10] could be obtained (i.e., 100 ppm) the first-order QED corrections could be tested but, as

is the case with the ground-state measurements, further improvements would be required to test higher-order corrections.

V. CONCLUSIONS

We have described a measurement of the fluorescence decay rate of $2\,^3P_J$ states of Ps that uses a Stark mixing scheme, analogous to the Zeeman mixing methods used to measure the fast annihilation decay rate of p-Ps [15]. We obtain $\Gamma_{\rm fl} = 299 \pm 25\,\mu{\rm s}^{-1}$, which is consistent with the theoretical value but is insufficient to test any QED corrections to the first-order (Bohr) energy levels [3]. The ∼8% precision of this measurement could be reduced with various improvements to the methodology, including initial state selection, using slower Ps atoms, microwave-induced quenching, and a large-area γ-ray detector. Nevertheless, this work shows conclusively that the Stark mixing scheme we have outlined is feasible.

ACKNOWLEDGMENTS

We are grateful to L. Liszkay for providing silica samples, to S. D. Hogan for assistance with the Stark-mixing calculations, to S. H. Reeder for assistance running the positron beamline, to D. M. Newson for useful discussions, and to J. Dumper and R. Jawad for technical assistance. This work was supported by the EPSRC under Grant No. EP/W032023/1.

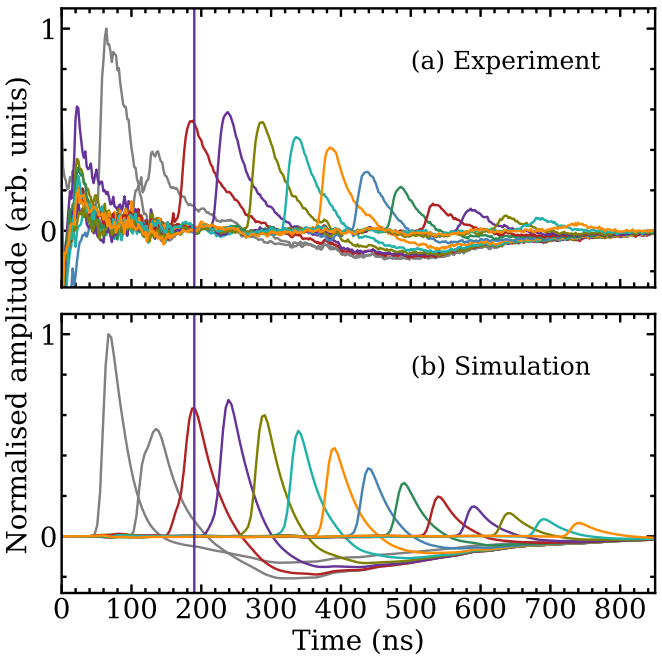

FIG. 7. (a) Measured and (b) simulated Rydberg peaks generated by field ionization at various times. The simulated data were obtained using $W_{\rm frac} = 2.4$. The interval between ionization pulse times was 50 ns, with the vertical line indicating a pulse applied at $t_Q = 190$ ns, the quenching time used in the $2\,S^*$ measurements.

APPENDIX: DETERMINATION OF v_z

The longitudinal Ps velocity distribution v_z was obtained by comparing measured time-delayed Rydberg field ionization data with simulations that include different test velocity distributions. Previous experiments using guided Rydberg Ps atoms [36] give an indication of the longitudinal Ps velocity spread, but this is not expected to be identical to the distribution present in the current experiment because the electrostatic ring guide used has a different phase-space acceptance and preferentially selects slower atoms. The transverse velocity distributions v_x and v_y are known from direct measurements, as described in Sec. II.

Rydberg atoms with principal quantum number $n = 23$ were generated using a two-photon, two-color excitation scheme [26] as described in Sec. II. The Rydberg atoms generated in this process have negligible annihilation decay rates, and their radiative lifetime is more than 40 μs [12], meaning that negligible loses are expected on the time scale of the experiment. Since the velocity distributions of the excited-state atoms are largely determined by the underlying ground-state distributions and the UV excitation laser properties, the Rydberg and $2\,^3S_1$ atom velocity distributions will be almost identical [34].

The number of Rydberg atoms present at different times was measured by rapidly turning on an electric field by applying a positive bias to electrode E1 using a fast high-voltage switch. This pulse was sufficient to field ionize all Rydberg atoms present in the LER and FMR regions [28], generating a signal with a magnitude proportional to the number of atoms present at the time of the pulse, as shown in Fig. 7(a). This process is similar to the quenching detection of $2\,S^*$ atoms described in Sec. II, except here the ionized Rydberg atoms are detected almost immediately.

The peak structure observed in the experiment represents the number of Rydberg atoms present in the LER and FMR as a function of time. The initial peak is large because most atoms are present in the LER at this time. After ionization the liberated positrons are returned to the target electrode and are all detected. After atoms pass through electrode E1 the peak amplitude falls, because liberated positrons may pass through the aperture in electrode E2 and are less efficiently detected. After some time, however, the x and y displacements increase such that positrons released by ionization strike electrode E2 and are detected. As time progresses, atoms travel out of the FMR, and some are lost via collisions with electrode E2 (see Fig. 3), again reducing the amplitude of the ionization peak.

Trajectory simulations incorporating the known v_x and v_y distributions, and the previously measured trial v_z distribution [36], were used to calculate the position of Ps atoms as a function of time (see Sec. III). Leapfrog propagation of 10 000 Rydberg atoms was performed using a velocity Verlet algorithm [44,45] in the geometry and electric fields of the experiment. This made it possible to track the atom positions, taking into account any acceleration caused by electric field gradients [36], and to determine how many atoms were lost due to collisions with the electrodes. In the simulations, ionizing electric fields were applied at varying times, and the resulting annihilation signals are shown in Fig. 7(b). The measured and simulated Rydberg ionization peak areas were compared, integrated as described in Sec. IV, and used to determine the v_z distribution present in the current apparatus.

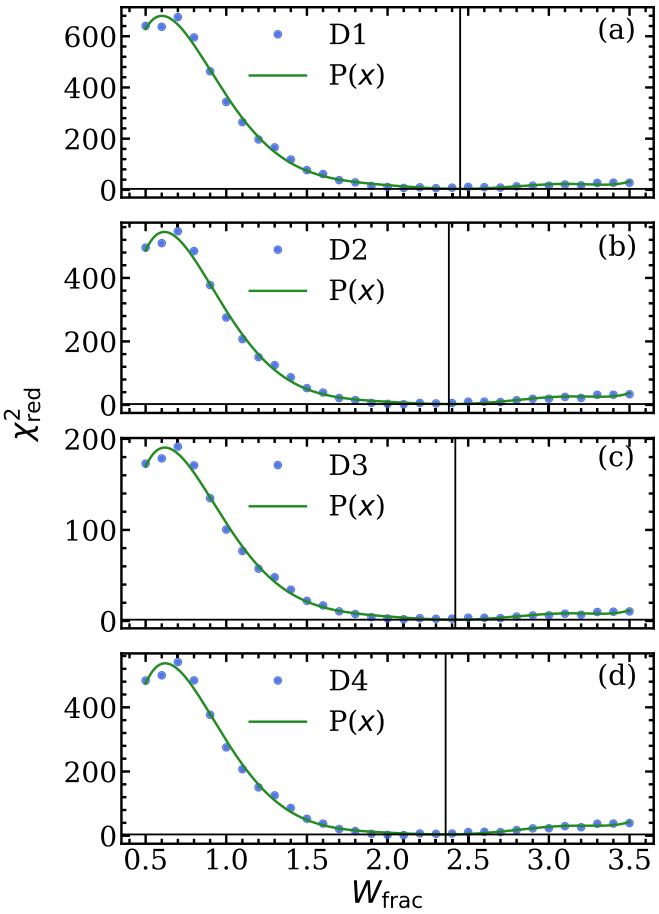

FIG. 8. χ^2_{red} as a function of W_{frac} as obtained for all gamma ray detectors (D1–D4). Here, $W_{\text{frac}} = 1$ corresponds to the initial trial function v_z distribution as described in the text. A seventh-order polynomial was fit to the data to determine the minima of the data sets. The solid vertical and horizontal lines indicate the minima of each fit.

The measured and simulated Rydberg data were directly compared via the reduced chi-squared parameter χ^2_{red} (see Sec. IV). The first two peaks in Fig. 7 (shown in gray) were not used in the calculation of the χ^2_{red} as they were used for normalization of the following peaks. An initial trial v_z distribution was obtained from a previous measurement of guided Rydberg Ps atoms, characterized by an asymmetric Gaussian function [36]. The guide used in that work had a lower phase acceptance than the electrode structure used in the current work, and the trial distribution was modified by adjusting the width of the asymmetric Gaussian function to account for the difference. The fractional width was defined by the parameter W_{frac}, where $W_{\text{frac}} = 1$ corresponds to initial trial distribution. This parameter was adjusted, and the resulting values of χ^2_{red} as a function of W_{frac} were determined, as shown in Fig. 8.

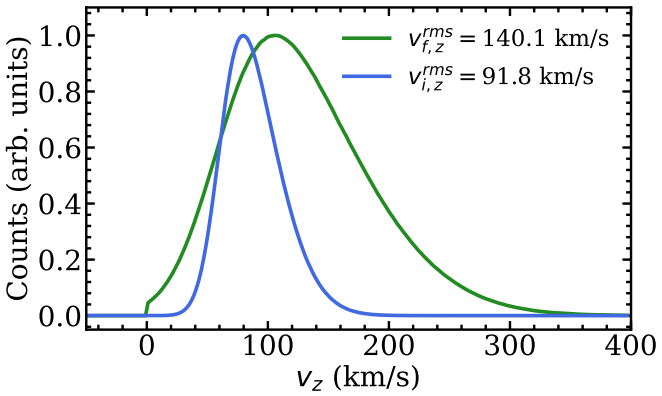

FIG. 9. The v_z velocity distributions of excited-state Ps atoms obtained from the ring-guide experiments ($v_{z,i}$, the trial distribution), and after the Rydberg ionization adjustment ($v_{z,f}$), as described in the text. The rms velocities for each distribution are indicated in the legend.

The v_z distribution which produced the best match to the experimental data (i.e., that for which χ^2_{red} was minimized as determined by a seventh-order polynomial, chosen using the same method described in Sec. IV) is shown in Fig. 9. This was taken as representing the experimental distribution, and was used for subsequent $2\,^3S_1$ simulations. We note that the distributions are truncated at $v_z = 0$ since Ps atoms traveling backward are not generated in the experiment. The average value of W_{frac} from the four detectors shown in Fig. 8 was $W_{\text{frac}} = 2.4$.

[1] J. A. Wheeler, Polyelectrons, Ann. N.Y. Acad. Sci. **48**, 219 (1946).

[2] S. G. Karshenboim, Precision study of positronium: Testing bound state QED theory, Int. J. Mod. Phys. A **19**, 3879 (2004).

[3] G. S. Adkins, D. B. Cassidy, and J. Pérez-Ríos, Precision spectroscopy of positronium: Testing bound-state QED theory and the search for physics beyond the standard model, Phys. Rep. **975**, 1 (2022).

[4] R. E. Sheldon, T. J. Babij, S. H. Reeder, S. D. Hogan, and D. B. Cassidy, Precision microwave spectroscopy of the positronium $2\,^3S_1 \rightarrow 2\,^3P_2$ interval, Phys. Rev. Lett. **131**, 043001 (2023).

[5] M. S. Fee, A. P. Mills, Jr., S. Chu, E. D. Shaw, K. Danzmann, R. J. Chichester, and D. M. Zuckerman, Measurement of the positronium 1^3S_1-2^3S_1 interval by continuous-wave two-photon excitation, Phys. Rev. Lett. **70**, 1397 (1993).

[6] A. Rich, Recent experimental advances in positronium research, Rev. Mod. Phys. **53**, 127 (1981).

[7] C. I. Westbrook, D. W. Gidley, R. S. Conti, and A. Rich, New precision measurement of the orthopositronium decay rate: A discrepancy with theory, Phys. Rev. Lett. **58**, 2153(E) (1987).

[8] R. S. Vallery, P. W. Zitzewitz, and D. W. Gidley, Resolution of the orthopositronium-lifetime puzzle, Phys. Rev. Lett. **90**, 203402 (2003).

[9] O. Jinnouchi, S. Asai, and T. Kobayashi, Precision measurement of orthopositronium decay rate using SiO_2 powder, Phys. Lett. B **572**, 117 (2003).

[10] Y. Kataoka, S. Asai, and T. Kobayashi, First test of $O(\alpha^2)$ correction of the orthopositronium decay rate, Phys. Lett. B **671**, 219 (2009).

[11] R. E. Sheldon, T. J. Babij, B. A. Devlin-Hill, L. Gurung, and D. B. Cassidy, Measurement of the annihilation decay rate of $2\,^3S_1$ positronium, Europhys. Lett. **132**, 13001 (2020).

[12] A. Deller, A. M. Alonso, B. S. Cooper, S. D. Hogan, and D. B. Cassidy, Measurement of Rydberg positronium fluorescence lifetimes, Phys. Rev. A **93**, 062513 (2016).

[13] E. D. Theriot, R. H. Beers, and V. W. Hughes, Precision redetermination of the hyperfine structure interval of positronium, Phys. Rev. Lett. **18**, 767 (1967).

[14] D. W. Gidley, A. Rich, E. Sweetman, and D. West, New precision measurements of the decay rates of singlet and triplet positronium, Phys. Rev. Lett. **49**, 525 (1982).

[15] A. H. Al-Ramadhan and D. W. Gidley, New precision measurement of the decay rate of singlet positronium, Phys. Rev. Lett. **72**, 1632 (1994).

[16] H. A. Bethe and E. E. Salpeter, *Quantum Mechanics of One- and Two-Electron Atoms* (Springer, Berlin, 1957).

[17] A. I. Alekseev, Two-photon annihilation of positronium in the P-state, Soviet Phys. JETP. **7**, 826 (1958).

[18] A. I. Alekseev, Three-photon annihilation of positronium in the P-state, Soviet Phys. JETP. **9**, 1312 (1959).

[19] A. M. Alonso, B. S. Cooper, A. Deller, S. D. Hogan, and D. B. Cassidy, Positronium decay from $n = 2$ states in electric and magnetic fields, Phys. Rev. A **93**, 012506 (2016).

[20] B. S. Cooper, A. M. Alonso, A. Deller, T. E. Wall, and D. B. Cassidy, A trap-based pulsed positron beam optimised for positronium laser spectroscopy, Rev. Sci. Instrum. **86**, 103101 (2015).

[21] A. P. Mills, Jr. and E. M. Gullikson, Solid neon moderator for producing slow positrons, Appl. Phys. Lett. **49**, 1121 (1986).

[22] J. R. Danielson, D. H. E. Dubin, R. G. Greaves, and C. M. Surko, Plasma and trap-based techniques for science with positrons, Rev. Mod. Phys. **87**, 247 (2015).

[23] A. P. Mills, Jr., Time bunching of slow positrons for annihilation lifetime and pulsed laser photon absorption experiments, Appl. Phys. **22**, 273 (1980).

[24] L. Liszkay, C. Corbel, P. Perez, P. Desgardin, M. F. Barthe, T. Ohdaira, R. Suzuki, P. Crivelli, U. Gendotti, A. Rubbia, M. Etienne, and A. Walcarius, Positronium reemission yield from mesostructured silica films, Appl. Phys. Lett. **92**, 063114 (2008).

[25] A. M. Alonso, S. D. Hogan, and D. B. Cassidy, Production of $2\,^3S_1$ positronium atoms by single-photon excitation in an electric field, Phys. Rev. A **95**, 033408 (2017).

[26] D. B. Cassidy, T. H. Hisakado, H. W. K. Tom, and A. P. Mills, Jr., Efficient production of Rydberg positronium, Phys. Rev. Lett. **108**, 043401 (2012).

[27] T. F. Gallagher, *Rydberg Atoms* (Cambridge University, Cambridge, 1994).

[28] A. M. Alonso, L. Gurung, B. A. D. Sukra, S. D. Hogan, and D. B. Cassidy, State-selective electric-field ionization of Rydberg positronium, Phys. Rev. A **98**, 053417 (2018).

[29] D. B. Cassidy, P. Crivelli, T. H. Hisakado, L. Liszkay, V. E. Meligne, P. Perez, H. W. K. Tom, and A. P. Mills, Jr., Positronium cooling in porous silica measured via Doppler spectroscopy, Phys. Rev. A **81**, 012715 (2010).

[30] T. E. Wall, A. M. Alonso, B. S. Cooper, A. Deller, S. D. Hogan, and D. B. Cassidy, Selective production of Rydberg-Stark states of positronium, Phys. Rev. Lett. **114**, 173001 (2015).

[31] A. Deller, B. S. Cooper, T. E. Wall, and D. B. Cassidy, Positronium emission from mesoporous silica studied by laser-enhanced time-of-flight spectroscopy, New J. Phys. **17**, 043059 (2015).

[32] D. B. Cassidy, S. H. M. Deng, H. K. M. Tanaka, and A. P. Mills, Jr., Single shot positron annihilation lifetime spectroscopy, Appl. Phys. Lett. **88**, 194105 (2006).

[33] A. M. Alonso, B. S. Cooper, A. Deller, and D. B. Cassidy, Single-shot positron annihilation lifetime spectroscopy with LYSO scintillators, Nucl. Instrum. Methods Phys. Res. Sect. A **828**, 163 (2016).

[34] D. B. Cassidy, Experimental progress in positronium laser physics, Eur. Phys. J. D **72**, 53 (2018).

[35] A. Deller, A. M. Alonso, B. S. Cooper, S. D. Hogan, and D. B. Cassidy, Electrostatically guided Rydberg positronium, Phys. Rev. Lett. **117**, 073202 (2016).

[36] M. H. Rayment, L. Gurung, R. E. Sheldon, S. D. Hogan, and D. B. Cassidy, Multiring electrostatic guide for Rydberg positronium, Phys. Rev. A **100**, 013410 (2019).

[37] E. Koehler, E. Brown, and S. J.-P. A. Haneuse, On the assessment of Monte Carlo error in simulation-based statistical analyses, Am. Statis. **63**, 155 (2009).

[38] Simion software, https://simion.com/.

[39] J. L. Devore, *Probability and Statistics for Engineering and the Sciences*, 8th ed. (Brooks/Cole, Boston, 2012).

[40] P. Mohr, E. Tiesinga, D. Newell, and B. Taylor, Codata Internationally Reconmmended 2022 Values of the Fundamental Physical Constants, Codata Internationally Reconmmended 2022 Values of the Fundamental Physical Constants, https://physics.nist.gov/constants.

[41] L. Gurung, T. J. Babij, J. Pérez-Ríos, S. D. Hogan, and D. B. Cassidy, Observation of asymmetric line shapes in precision microwave spectroscopy of the positronium $2\,^3S_1 \rightarrow 2\,^3P_J$ ($J = 1, 2$) fine-structure intervals, Phys. Rev. A **103**, 042805 (2021).

[42] T. R. Weber, J. R. Danielson, and C. M. Surko, Electrostatic beams from tailored plasmas in a Penning-Malmberg trap, Phys. Plasmas **17**, 123507 (2010).

[43] L. Gurung, T. J. Babij, and D. B. Cassidy, Fast decay of $2\,^3S_1$ positronium atoms in an MgO lined cavity, EPJ Tech. Instrum. **8**, 3 (2021).

[44] M. E. Tuckerman, *Statistical Mechanics: Theory and Molecular Simulation* (Oxford University, Oxford, 2010), pp. 100–101.

[45] R. J. Sadus, *Molecular Simulation of Fluids: Theory, Algorithms and Object-Orientation* (Elsevier, Oxford, 2002), pp. 228–229.